Semi-Interpenetrating Network Electrolytes Utilizing Ester-Functionalized Low T_g Polysiloxanes in Lithium-Metal Batteries

Jannik Petry, Markus Dietel, and Mukundan Thelakkat*

Solid polymer electrolytes (SPE) obtained from polyesters are viable alternatives to polyethylene oxide-based materials, especially for room-temperature applications. In SPEs, the ion conduction is dependent on the polymer segmental mobility and is thus facilitated by low glass transition temperature (T_g). Here, the study synthesizes an ester-funtionalized polysiloxane-based polymer electrolyte with an exceptionally low T_g of −76 °C, resulting in a high ionic conductivity of 2.6×10^{-5} S cm^{-1} at room temperature and a lithium transference number of 0.72. However, the low T_g and consequently low mechanical stability require reinforcement to promote the formation of stable lithium-electrolyte interfaces in lithium plating stripping experiments and stable battery cycling in lithium-metal batteries (LMBs). For this, the SPE is incorporated into a network structure to yield a semi-interpenetrating network electrolyte (SPE20-SIPN) which results in significantly improved storage modulus by three orders of magnitude and ionic conductivity is maintained upon crosslinking. The SPE20-SIPN exhibits stable cycling for up to 50 cycles with fluctuation (voltage noise) in some of the cells. A combination of crosslinking and nanoparticle addition (SPE20-N10-SIPN) overcomes the voltage noise and results in high coulombic efficiencies and high capacity retention above 80% for 200 cycles in solvent-free, all-solid-state LMBs at 30 °C.

1. Introduction

Batteries are driving electronic devices in a multitude of applications and different ranges of current and potential requirements. Especially for mobile applications, in electric vehicles, or portable power stations, the energy density of the battery is a deciding aspect for its integration. Current state-of-the-art lithium-ion batteries (LIBs) are reaching their theoretical energy density limit, requiring new concepts for further improvements.[1] In Lithium-metal batteries, elemental lithium (Li^0) substitutes typical graphite anodes and thereby promises a significantly improved specific capacity by up to ten times. However, the Li-metal anodes also require new electrolyte systems, as the liquid systems employed in LIBs are not compatible with the lithium anodes and tend to form uneven and dendritic lithium growth during battery operation.[2–5] Solid polymer electrolytes (SPEs), describing dry (i.e., non-swollen, solvent-free) mixtures of polymer matrixes and lithium-salts, are one potential candidate to be applied in LMBs. In the field of SPEs, poly(ethylene oxide) (PEO) has dominated the research focus with different polymer architectures, copolymers, and additives tested to overcome some inherent challenges linked to its application as SPE.[6,7] Namely, the high degree of crystallization limits the ionic conductivity at temperatures below its melting point (T_m) of ≈65 °C. In addition, the electrochemical stability of only up to 4.6 V also limits the applicability of PEO in combination with high-voltage cathode systems. Furthermore, the strong coordination free electron pairs of the ether-oxygen to lithium cations restricts the cation mobility, resulting in low lithium transference numbers (LTN, t_{Li^+}) between 0.1–0.3.[8,9] The low LTN can manifest in pronounced ion concentration gradients during cycling.[8,10,11]

Alternatives to polyether-based electrolytes are commonly summarized as beyond-PEO materials which include, e.g., polyesters and polycarbonates. In polyester-based materials like poly(ϵ-caprolactone) (PCL) the coordination of lithium cation is mostly through carbonyl-oxygen (C=O) atoms.[12,13] The C=O—Li$^+$ interaction is significantly weaker, resulting in considerably improved t_{Li^+} to values above 0.5.[9,14,15] Polyesters also persist a higher oxidative stability of up to 4.8 V revising the library of applicable cathode materials. However, similarly to PEO, PCL is

J. Petry, M. Dietel, M. Thelakkat
Applied Functional Polymers
University of Bayreuth
Universitätsstraße 30, 95447 Bayreuth, Germany
E-mail: mukundan.thelakkat@uni-bayreuth.de
M. Thelakkat
Bavarian Center for Battery Technology (BayBatt) and Bavarian Polymer Institute (BPI)
University of Bayreuth
Universitätsstraße 30, 95447 Bayreuth, Germany

**ADVANCED
SCIENCE NEWS**

www.advancedsciencenews.com

**ADVANCED
ENERGY
MATERIALS**

www.advenergymat.de

semi-crystalline and therefore suffers from low ionic conductivity below its melting T_m of ≈56 °C.[12] In general, different synthetic approaches for polyesters have been applied to improve both the overall ionic conductivity as well as at room temperature.[16–20] Recently, we demonstrated the successful use of poly(meth-)acrylate-based SPEs with different diester side chains. The amorphous materials showed high ionic conductivities even at lower temperatures. Similar to commonly observed trends, the series of diester polymers also showed a distinct scaling of the ionic conductivity with the glass transition temperature of the different polymer electrolytes: higher ionic conductivities being accessible with low T_g electrolyte systems. [12,13,21]

Herein, we present a pathway to further decrease the glass transition temperature of ester-functionalized polymer electrolytes for improved ionic conductivity properties. The polysiloxanes backbone shows some of the lowest accessible glass transition temperatures due to the high backbone flexibility. In polysiloxanes, depending on their substitution pattern of the polymer backbone, many different functionalities and therefore properties can be tailored by the selection of side chain motifs.[22–24]

However, the very low T_g polysiloxane electrolytes come with the challenge of maintaining mechanical stability of the electrolyte. A certain mechanical integrity and softness of the electrolytes is essential to establish a stable lithium-electrolyte interface and to prevent an uncontrolled and/or dendritic lithium deposition upon cycling.[17] Cross-linking is a common strategy to enhance the mechanical properties of an electrolyte. Here we want to distinguish between systems where a) a polymer electrolyte contains reactive functional groups, which form a network structure on its own or with an additional crosslinker (elastormers/duroplasts) and b) the polymer electrolyte (without reactive groups) is entrapped in an external network structure (semi-interpenetrating networks, SIPNs). In both cases, the crosslinked structure can increase the Young's modulus or the mechanical properties of the polymer electrolyte in general. For the former approach, reported works used bifunctionalized oligoethylene glycols (OEG) as crosslinkers. [25–27] One of the most widely studied crosslinked systems involving polysiloxane consists of a oligoethylene glycol- functionalized poly(siloxane-g-ethylene oxide). Here, short OEG telechelics were used as crosslinker, but detailed interface impedance or plating/stripping and battery cycling data is not available for this system.[26,28,29] In the field of SIPNs different combinations of polyether-based electrolytes and networks have been demonstrated.[30–33] The SIPN strategy does not demand the functionalization of the polymer electrolyte with reactive groups and any polymer electrolyte can be incorporated into a variety of in-situ formed network structures.

To realize a full polyester-based SIPN, we synthesized a new polysiloxane carrying pendent diester side chains. Further, we used a polyester-based telechelic diacrylate instead of OEG telechelics as crosslinker. As both constituents only feature ester moieties, high LTNs can be expected. First, we studied the electrolyte characteristics of the polysiloxane-based SPE. Then the SPE is combined with the crosslinker that can be cured in situ inside the test cells to obtain SPE-SIPN electrolytes, providing both high ionic conductivity, high LTN, and improved mechanical stability. We investigated the influence of the network formation on the ion transport, mechanical properties, as well as the

stability and reversibility of the lithium-electrolyte interface. Both the mechanical and interfacial stability could be significantly improved in the SPE20-SIPN, while maintaining high ionic conductivity. Furthermore, the charge/discharge and cycling performance was studied using Li|electrolyte|lithium iron phosphate (LFP) test cells demonstrating good discharge capacities at 30 °C its high retention after 200 cycles.

2. Results and Discussion

2.1. Material Synthesis

Two different polymers have been synthesized for this work: a polysiloxane with pendent diester side chains (poly(methyl-[butyl-4-{methyl adipate}])siloxane, PM(BMA)S and a polycaprolactone diacrylate telechelic (poly(caprolactone) diacrylate, PCLDA) as crosslinker. The syntheses, monomers/intermediates, and polymers are illustrated in **Figure 1**a. Due to a variety of possible functional olefins, tailored functional polysiloxanes are accessible from poly(methylhydro)siloxane (PMHS). The PM(BMA)S was synthesized utilizing the Karstedt's catalyst in a hydrosilylation reaction between commercially available PMHS and synthesized but-3-en-methyl adipate (BM3A) to be used as side chain. The hydrosilylation reaction involves an Pt-catalyzed olefin addition to the PMHS backbone. For synthetic details of BM3A refer to the Supporting Information. The PM(BMA)S and PCLDA are later combined to form the SIPN structure by radical polymerization (Figure 1b). The reactions were monitored using ¹H NMR spectroscopy (Figure 1c). For PM(BMA)S the quantitative side chain addition can be observed by the diminished proton signal of PM*H*S at 4.7 ppm.

The low-molecular weight PCLDA crosslinker was synthesized by an esterification reaction of commercially available polycaprolactone diol (PCLD, M_n 3300 g mol⁻¹) with acryloyl chloride. Here, the introduction of the polymerizable acrylate moieties can be traced by the appearance of $H_2C=CH$-R double bond proton signals (6.5–5.5 ppm) and the shifted proton signal for the PCL-CH_2-OH (shifted from 3.6 to 4.1 ppm) due to the esterification reaction. Detailed peak assignment can be found in the supporting information (Figures S1–S3, Supporting Information). The addition of B3MA and the acrylate moiety can be further observed in SEC measurements (Figure 1d). As the BMA side chain constitutes a large proportion of the PM(BMA)S the shift of molecular weight is more pronounced than for PCLDA as only the end groups of PCLD are functionalized. The commercial PMHS shows a bimodal molecular weight distribution, which can not be observed in the synthesized PM(BMA)S.

Thermal characterization was conducted by thermogravimetric analysis (TGA) and differential scanning calorimetry (DSC) (Figures S4–S6, Supporting Information). Both PM(BMA)S and PCLDA show significantly higher thermal stability than the respective precursor materials and with that sufficient thermal stability for battery applications. The incorporation of diester side chains in PM(BMA)S resulted in a drastic increase of the glass transition temperature (T_g) to −76 °C compared to −138 °C for PMHS. With that, PM(BMA)S still undercuts the T_g of commonly used linear poly(ethylene oxide) (PEO) $T_{g,PEO}$ = −50 °C and linear poly(ϵ-caprolactone) (PCL) $T_{g,PCL}$ = −65 °C.[34,35]

**ADVANCED
SCIENCE NEWS**

www.advancedsciencenews.com
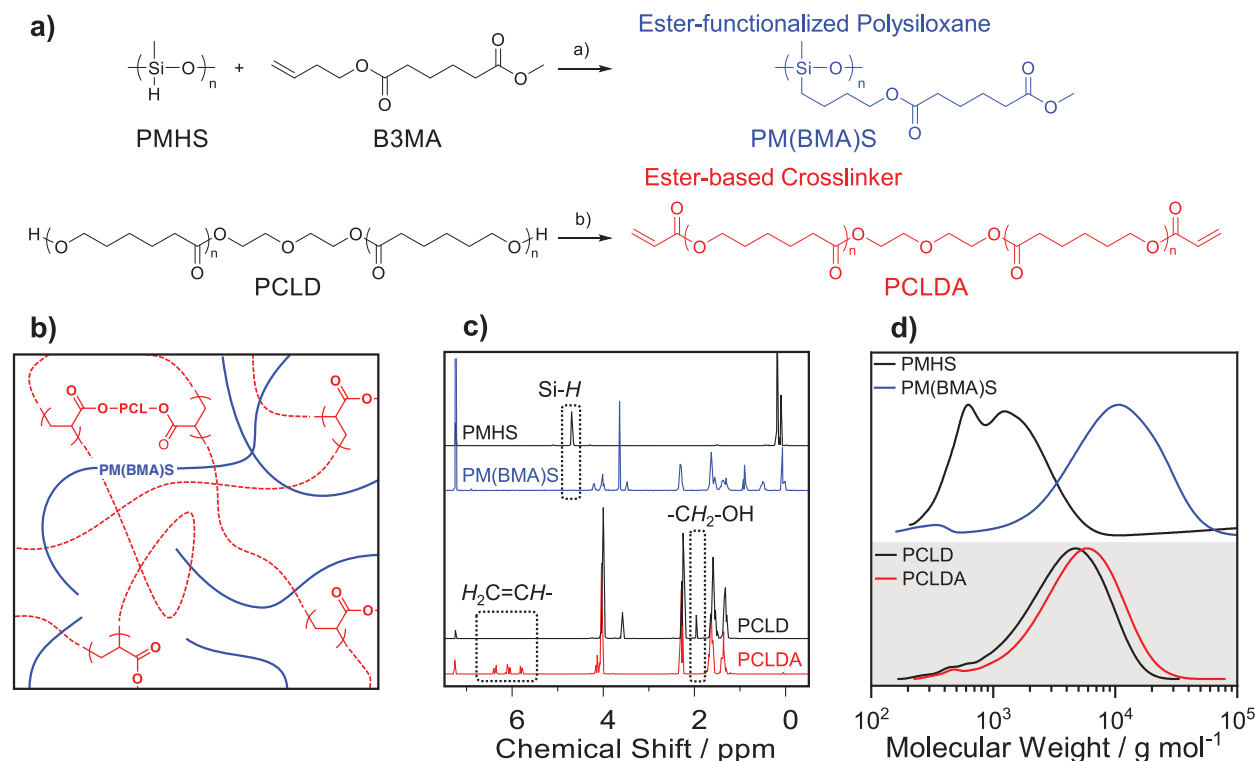
**ADVANCED
ENERGY
MATERIALS**

www.advenergymat.de

Figure 1. a) Reaction scheme for the synthesis of (top) the siloxane-based polymer electrolyte PM(BMA)S and (bottom) the polycaprolactone-based network former PCLDA. b) Schematic illustration of the SIPN structure obtained from PM(BMA)S and PCLDA. c) ^{1}H NMR spectra of the products and the respective precursors. d) Molecular weight distributions determined by size-exclusion chromatography (THF+0.25 wt.% TBAB, PS calibration).

Furthermore, PM(BMA)S is amorphous and exhibits no further thermal transitions. Contrarily, both PCLD and PCLDA show distinct melt and crystallization transitions typical for linear poly(caprolactone)s. An overview of molecular weights, polymer dispersity, and thermal properties is given in **Table 1**.

2.2. Ionic Conductivity and Characteristics

The synthesized PM(BMA)S is converted to a solid polymer electrolyte (SPE10-50, Digits = LiTFSI wt.%) by the addition of LiTFSI (Table S1, Supporting Information). The ionic conductivity of the obtained SPEs was characterized by electrochemical impedance spectroscopy (EIS) at various temperatures and salt

concentrations between 10 and 50 wt.% in symmetrical stainless steel cells (StSt|electrolyte|StSt). Individual EIS measurements were evaluated by the general distribution of relaxation times (gDRT) giving access to the bulk resistance and thus the ionic conductivity of the polymer electrolytes. Details of the DRT method and analysis are published by us in earlier works.[12,13,37] In DRT, electrochemical processes are transduced from the frequency into the time domain. Thereby, processes can be individually observed and clearly distinguished by their relaxation time constant (τ). The ionic conductivity was calculated by Equation (1) based on the determined bulk resistance (R_b) and with the electrolyte geometry (L thickness of the electrolyte, A area of the electrolyte).

$$\sigma = \frac{L}{R_b \cdot A} \tag{1}$$

The corresponding Arrhenius plots of the determined conductivities are depicted in **Figure 2a**. The corresponding impedance spectra are shown in Figure S7 (Supporting Information).

The polymer electrolytes do not show strict Arrhenius behavior (i.e., a linear temperature dependence) but a curved temperature dependence described by the Vogel–Tammann–Fulcher-(VTF)-model. In addition to an Arrhenius-type temperature dependence, the VTF-model accounts for the dependence of the ionic conductivity on the segmental mobility commonly observed in polymer electrolytes. This correlation results in the typical curved dependencies. The determined conductivity data was

Table 1. Overview of the molecular weights and thermal properties of the synthesized polymers and their respective precursors.

Polymer	M_n [a]	$Đ$ [b]	$T_{d,5\%}$ [c] [°C]	T_g [c] [°C]	T_{cry} [c] [°C]	T_m [c] [°C]	ΔH_m [c] [J g^{-1}]
PMHS	900	1.6	212	−138[d]	–	–	–
PM(BMA)S	7400	1.8	351	−76	–	–	–
PCLD	2400	2.0	258	–	35	48	83.4
PCLDA	3300	2.0	303	–	26	44	77.6

[a] determined by SEC, eluent: THF + 0.25 wt.% TBAB, PS calibration; [b] based on SEC results: M_w/M_n; [c] determined from the second heating or cooling curve (10 K min^{-1}); [d] value taken from literature.[36]

**ADVANCED
SCIENCE NEWS**

www.advancedsciencenews.com

**ADVANCED
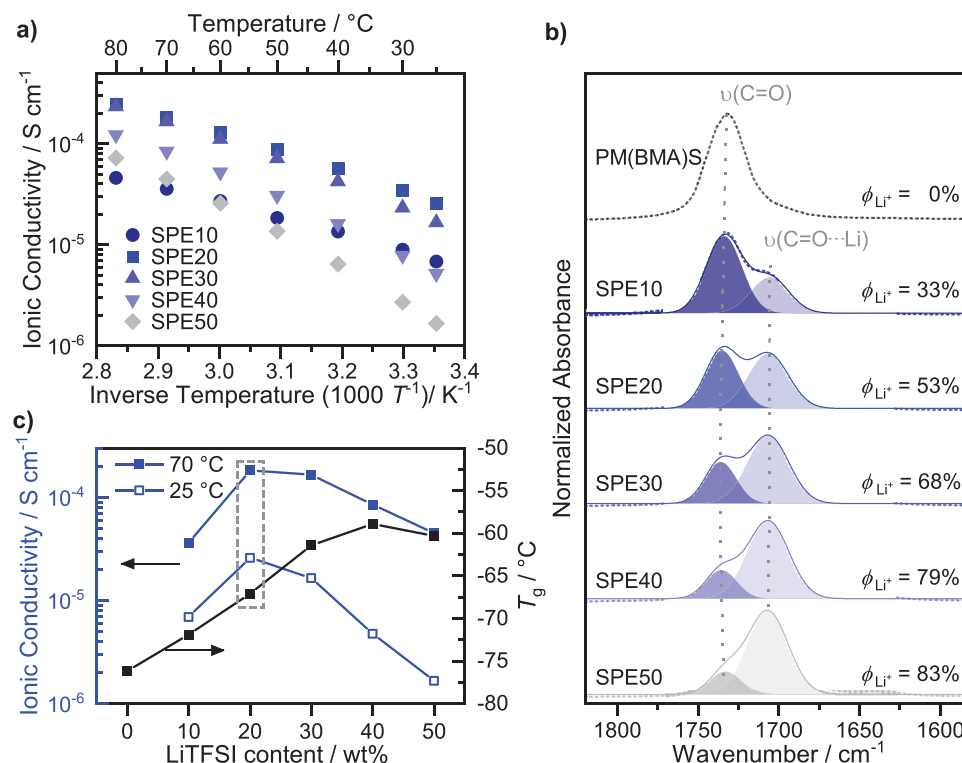ENERGY
MATERIALS**

www.advenergymat.de

Figure 2. a) Arrhenius plots of the temperature-dependent ionic conductivity measurements of SPEs with different LiTFSI salt concentrations between 10 and 50 wt.%. b) (dotted lines) recorded FT-IR spectra, (solid lines) cumulative fit, (dark shared area) fit for $\nu(C{=}O)$-peak at 1730 cm^{-1} and (light shaded area) fir for $\nu(C{=}O{-}Li)$-peak at 1705 cm^{-1}. Each spectrum is normalized to the cumulative peak area. The fraction of coordinated carbonyl groups (ϕ_{Li^+}) is calculated as the ratio of $A_{\nu(C{=}O{-}Li)}/(A_{\nu(C{=}O)} + A_{\nu(C{=}O{-}Li)})$. c) LiTFSI salt concentration variation between 10 and 50 wt.%. (blue) Ionic conductivity at (squares) 70 °C, (hollow squares) 25 °C. (black) The glass transition temperature of the pristine polymer and the solid polymer electrolytes. Solid lines in (c) are a guide to the eye.

evaluated and fitted using the VTF model (Equation (2); Figure S8, Supporting Information). The VTF fit parameters are given in the supporting information Table S2 (Supporting Information).

$$\sigma = A \cdot exp\left(-\frac{B}{R\left(T - T_0\right)}\right) \qquad (2)$$

The prefactor A is mostly associated with the salt/charge carrier concentration in the electrolyte, while the VTF pseudo-activation energy (B) includes the segmental mobility. The ionic conductivity is not only dependent on the temperature of the measurement but also on the so-called Vogel temperature (T_0). As an estimation for polymer electrolytes, this T_0 is often defined as $T_0 = T_g - 50$ °C.[38] Hence, the observed electrolyte glass transition temperature (T_g) influences the ionic transport properties, even if the observed temperature range is considerably higher than the T_g. From the VTF fits, the dependence of the ionic conductivity on the charge carrier concentration and the activation energy can be deduced. The activation energy increases steadily with increasing salt concentration from SPE10 to SPE50 (Table S2, Supporting Information). Despite the electrolyte with 10 wt.% LiTFSI (SPE10) exhibiting the lowest activation energy, the overall ionic conductivity is limited by the low concentration of charge carriers. Only after the addition of 20–30 wt.% LiTFSI the charge carrier concentration is sufficient to ensure high ionic conductiv-

ities. At higher salt concentrations the ionic conductivity is then limited by the increasing activation energy (Table S2, Supporting Information). The highest room temperature ionic conductivity of 2.6×10^{-5} S cm^{-1} was observed at a salt concentration of 20 wt.% (**Table 2**).

In addition, the glass transition temperature (T_g) was determined by differential scanning calorimetry to correlate the T_g to the ionic conductivity (Figure S9, Supporting Information). Often, an optimum of the ionic conductivity is observed at salt concentrations establishing a sufficient concentration of charge carriers while retaining a low glass transition temperature for the electrolyte. With increasing salt concentration, the T_g was increased from −76 °C (for 0 wt.% salt) to a plateau at ≈−60 °C for SPE30-SPE50. In the case non-crosslinked SPE based on PM(BMA)S the best trade-off and the highest ionic conductivity could be observed for SPE20 at a salt concentration of 20 wt.% (corresponding to a molar ratio of carbonyl groups to added lithium ions of C═O/Li = 8.4) (Figure 2c).

Besides the overall ionic conductivity, the lithium transference number (t_{Li^+}) was determined to understand the contribution of the Li-ion conductivity of the total ionic conductivity. The evaluation was performed in accordance with the Bruce and Vincent method consisting of two electrochemical impedance spectra and an intermediate polarization period.[39] Based on the changes in the Li-electrolyte interface resistance before and after the polarization period as well as the current response

**ADVANCED
SCIENCE NEWS**

www.advancedsciencenews.com

**ADVANCED
ENERGY
MATERIALS**

www.advenergymat.de

Table 2. Overview of the glass transition temperature, achieved ionic conductivities and fraction of coordinating carbonyl groups for the electrolytes SPE10-50.

Electrolyte	LiTFSI [wt.%]	CO/Li	T_g [°C]	σ@25 °C [S cm^{-1}]	σ@70 °C [S cm^{-1}]	ϕ_{Li+} [%]
SPE10	10	18.9	−71.9	6.8×10^{-6}	3.6×10^{-5}	33
SPE20	20	8.4	−67.1	2.6×10^{-5}	1.8×10^{-4}	53
SPE30	30	4.9	−61.5	1.7×10^{-5}	1.7×10^{-4}	68
SPE40	40	3.1	−58.9	5.2×10^{-6}	8.4×10^{-5}	79
SPE50	50	2.1	−60.3	1.7×10^{-6}	4.5×10^{-5}	83

during the chronoamperometric polarization, a lithium transference number can be calculated (data and evaluation can be found in Figure S10 and Table S3, Supporting Information). For the SPE20 the LTN was determined as 0.72 ± 0.04, which is comparable with linear polycaprolactone (PCL).[12,40] A high transference number above 0.5 is desirable, so that the effective Li-ion conductivity constitutes a higher proportion of the overall ionic conductivity. Furthermore, possible polarization gradients due to an over-polarization of the counter anions (i.e., TFSI$^-$) can be reduced. Such gradients can impede effective charge transport and transfer reactions limiting the electrolyte performance.[11,41] The high LTN observed for ester-based electrolytes are in contrast to ether-based (e.g., PEO-based) electrolytes, where the strong Li-ion complexation by the free electron pairs of the ether oxygen atoms result in low transference numbers ≈0.1–0.3.[9]

Furthermore, the Li$^+$-carbonyl oxygen coordination was investigated by FT-IR spectroscopy for SPE10 to SPE50. The carbonyl stretching vibration region between 1600 and 1800 cm^{-1} is an indicator of the coordination environment between the carbonyl moieties and lithium ions. The PM(BMA)S without any Li-salt only exhibits one peak at 1734 cm^{-1} corresponding to the stretching vibration of the free carbonyl groups (ν(C=O)). Upon the addition of salt, a secondary peak arises at ≈1705 cm^{-1} which can be attributed to the stretching vibration of carbonyl groups taking part in lithium coordination (ν(C=O—Li)).[12] The IR signals were deconvoluted by nonlinear double-peak Gaussian fitting of the two peaks (Table S4, Supporting Information). The ratio of the resulting area (A) of the individual fits $A_{\nu(C=O)}$ and $A_{\nu(C=O—Li)}$ are used to determine the fraction of carbonyl groups involved in Li$^+$ coordination (ϕ_{Li+}). As observed in our previous studies the maximum ionic conductivity was observed for a ϕ_{Li+} of ≈50% indicating that an equal amount of complexing and free carbonyl groups are indicative for efficient ion transport.[12,13]

2.3. Semi-Interpenetrating Network – Ionic Conductivity and Rheology

So far we demonstrated, that the low glass transition temperature of the polysiloxane-based diester electrolyte translates well to high ionic conductivity, while the contributing ester-moieties result in high LTN. However, the pursuit of low-T_g, flexible, and soft polymer electrolytes faces problems with interfacial instabilities, as the consequence of low mechanical structural integrity and mechanical stability. Amongst other approaches, the use of network-forming polymers has been shown to improve mechan-

ical stability as well as cyclability.[42] Therefore, we employed the synthesized PCLDA crosslinker to establish a coherent framework to improve the mechanical stability of the electrolyte system. Exemplary optical images of SPE20 and SPE20-SIPN are depicted in Figure S11 (Supporting Information).

For further investigation, we utilize the crosslinker PCLDA in combination with the PM(BMA)S. The SPE20-SIPN is obtained by homogenously mixing PM(BMA)S, PCLDA, LiTFSI, and a radical initiator (azobisisobutyronitrile, AIBN) in solution. For the sake of comparability, the ester moieties of the PCLDA were taken into account for the calculation of the salt concentration. The total LiTFSI content was maintained at 20 wt.%, resulting in a comparable C=O/Li ratio of 8.9 (Table S5, Supporting Information). During cell preparation, the electrolytes were thoroughly dried and thermally crosslinked to yield semi-interpenetrating network structures (SPE20-SIPN). The effect of the network formation was evaluated by comparative ionic conductivity and rheological measurements (**Figure 3**).

The ionic conductivity of both the SPE20 and SPE20-SIPN were similar at temperatures above 40 °C. At lower temperatures, the network shows a marginally reduced ionic conductivity, most likely due to the restriction of polymer segmental mobility in the network structure. Based only on the polymeric constituents of SPE20-SIPN, the polymer matrix consists of ca. 55 wt.% PM(BMA)S and 45 wt.% PCLDA, respectively. Even though the network constitutes almost half of the ion-conducting matrix, the effective ionic conductivity is very similar to SPE20. Furthermore, the PCLDA and 20 wt.% of LiTFSI were used as network electrolyte without any PM(BMA)S. The network (PCLDA20) itself showed significantly reduced ionic conductivities over the whole temperature range and an ionic conductivity of 2.7×10^{-6} S cm^{-1} at 25 °C. The observed conductivities are in the same range as observed by Jalbert et al., who used the crosslinker as a 3D network electrolyte, as the crosslinker in combination with a Li-salt. The network showed a high Youngs's modulus of 5.5×10^6 Pa, however, the observed room temperature conductivity was 3.6×10^{-6} S cm^{-1} at a salt concentration of 40 wt.%.[43]

A comparison of a fully cross-linked polyester PLCDA20 with the SPE20-SIPN clearly indicates that a certain amount of segmental mobility is to be guaranteed in crosslinked electrolytes to achieve high ionic conductivities, especially at room temperature.

The effect of the network formation on the mechanical properties was evaluated by rheological measurements. Therefore, a non-crosslinked blend of PM(BMA)S and PCLDA and the corresponding cured and crosslinked semi-interpenetrating network were evaluated (Figure 3a, blend and network). The pure PM(BMA)S was not investigated individually, as we wanted
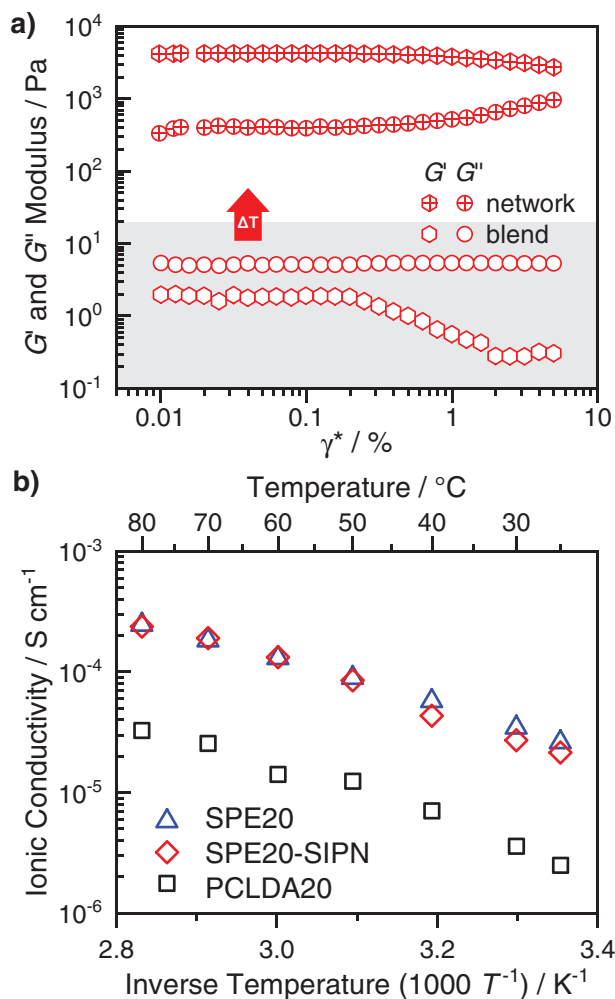
**ADVANCED
SCIENCE NEWS**

www.advancedsciencenews.com

**ADVANCED
ENERGY
MATERIALS**

www.advenergymat.de

Figure 3. a) Rheological strain sweep measurement at 1 Hz and 60 °C of (hollow symbols) the pristine blend of PM(BMA)S and PCLDA before crosslinking and (hashed symbols) the obtained network after thermal crosslinking. b) Temperature-dependent ionic conductivity of the SPE20 (PM(BMA)S + 20 wt.% LiTFSI), the crosslinked electrolyte (SPE20-SIPN), and the crosslinker electrolyte PCLDA20 (PCLDA + 20 wt.% LiTFSI) without the incorporation of the polysiloxane-based polymer.

2 Pa for the blend to 4250 pa for the network. In frequency-sweep measurements, the cured network system showed steady G' and G'' with $G' > G''$ across the frequency range, typical for crosslinked polymer systems. The non-cured mixture however exhibited different plateaus and transitions between viscous and elastic behavior, most likely related to the combination of two vastly different polymer structural domains.

In combination, the results from the ionic conductivity and rheological measurements underline the importance of adequate network design offering both mechanical stability while retaining a high ionic conductivity. Further studies on the applicability in context with lithium-metal batteries will be discussed in the following sections.

2.4. Electrochemical Stability Window and Lithium Compatibility

The electrochemical stability window (ESW) of the SPE20 was evaluated by linear sweep voltammetry in Li|SPE|StSt test cells (**Figure 4a**). The degradation potential $V_{d,LSV}$ was determined geometrically at the transition from the faradaic to the non-faradaic regime ($V_{d,geo}$) and as the potential where a threshold current density of 0.1 mA cm^{-2} ($V_{d,th}$) is reached.[44] Both methods result in similar decomposition values of 5.28 and 5.34 V for $V_{d,geo}$ and $V_{d,th}$, respectively. However, in LSV experiments the electrochemical stability is often overestimated as influences of the cathode electrolyte interface (CEI) are neglected.[45,46] Thus, we
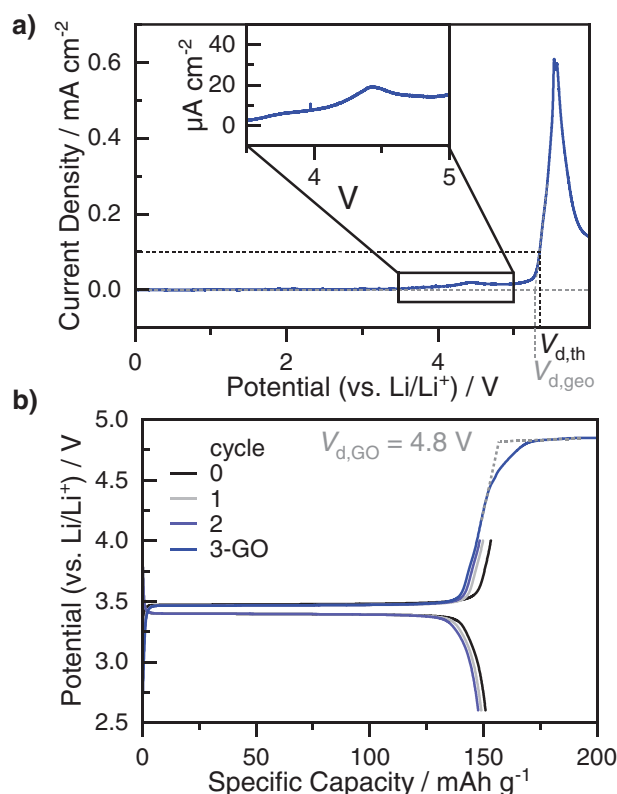

Figure 4. a) Linear sweep voltammetry of SPE20 using Li|SPE|StSt cells from 0 to 6 V at a sweep rate of 0.1 V s^{-1} at 70 °C. b) Galvanostatic overcharging in Li|SPE20|LFP cells at 70 °C at 0.1 C. Before charging without a cut-off potential, three cycles between 2.6 and 4.0 V are performed.
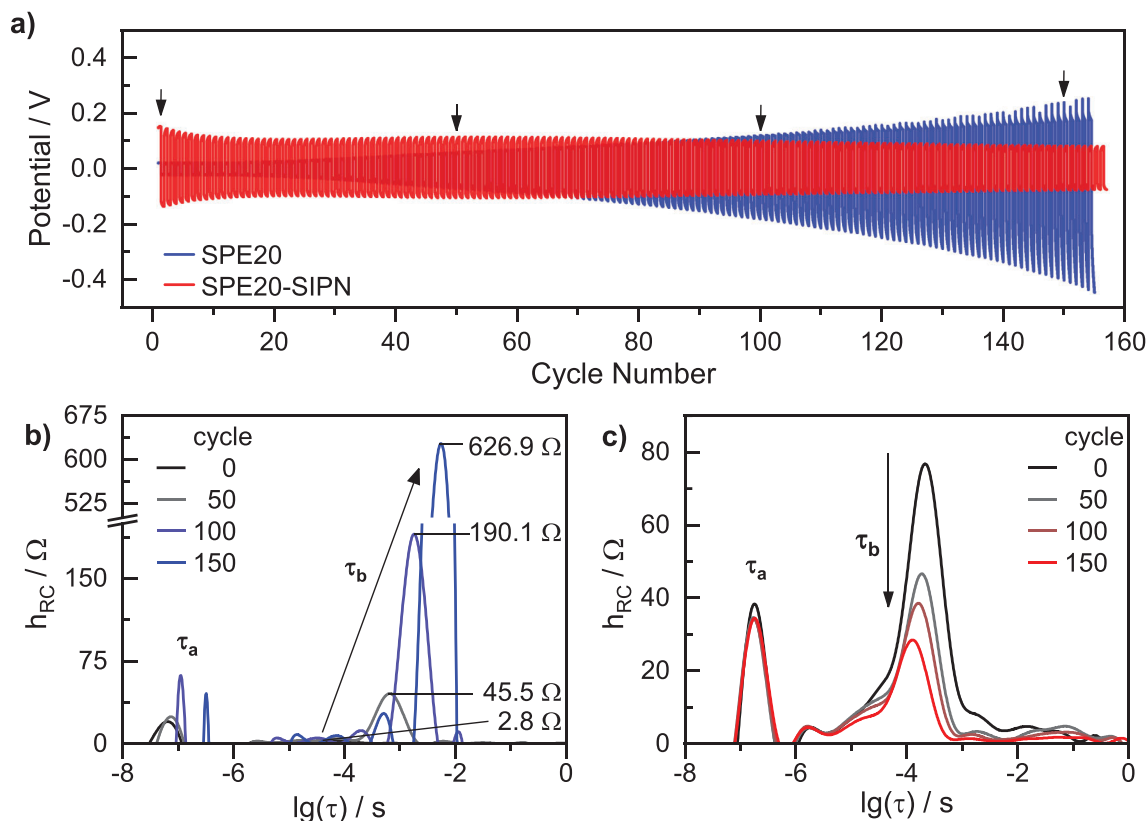
to evaluate the direct influence of the network formation by comparing the blend (before crosslinking) and network (after crosslinking). It should also be noted that we did not use any Li-salt during the rheology measurements, due to the hygroscopic nature under ambient conditions of measurements. The storage (G') and loss (G'') moduli were recorded during strain-sweep measurement (Figure 3a) and frequency sweep measurements (Figure S12, Supporting Information). Deviations from the linear viscoelastic regime (e.g., horizontal plateau) above an applied strain of 0.2% indicate the loss of structural integrity and nonreversible deformation of the polymer structure. The polymer blend shows predominantly viscous behavior with $G' < G''$. Upon SIPN formation the change to a predominantly elastic behavior ($G' > G''$) demonstrates the significant influence of the structure-giving PCLDA network. The storage modulus (at 0.1% strain) could be increased by more than three orders of magnitude from

**ADVANCED
SCIENCE NEWS**

www.advancedsciencenews.com

**ADVANCED
ENERGY
MATERIALS**

www.advenergymat.de

Figure 5. a) Lithium plating/stripping cycling data using Li|electrolyte|Li symmetrical cells (electrolyte thickness 136 µm, diameter 4 mm) at 70 °C using a half cycle time of 1 h and a current density of 0.1 mA cm^{-1}. Cycling data for (blue) SPE20 and (red) SPE20-SIPN. Arrows indicate the cycles analyzed by EIS and gDRT. b,c) gDRT analysis for the 0th, 50th, 100th, and 150th cycle. The results are represented by the absolute distribution function h(τ). Peaks τa and τb can be attributed to the ionic conductivity and the charge transfer processes, respectively.

conducted additional galvanostatic overcharging (GO) experiments in Li|SPE20|LFP cells mimicking the operational conditions of later battery cells. After three equilibration cycles, the battery was charged without a cut-off potential at 0.1C. The GO charging profile exhibits the LFP-typical plateau at 3.5 V with a distinct increase of the potential after completed charging. At 4.8 V a second plateau substantiates, marking the limit of oxidative stability ($V_{d,GO}$) under operational conditions (Figure 4b). The differences between $V_{d,LSV}$ and $V_{d,GO}$ demonstrate the importance of the evaluation of the electrochemical stability under operational conditions. The ESW of 4.8 V (vs Li/Li$^+$) could benefit the application of high-voltage cathode systems. However, we exclusively used LFP-based cathodes in this work.

To elaborate on the compatibility between lithium-metal electrodes and the synthesized PM(BMA)S as well as the obtained semi-interpenetrating network, we conducted lithium plating/stripping experiments in Li|electrolyte|Li symmetrical cells (**Figure 5a**). To attain a more in-depth understanding of the interfacial processes and changes we employed intermittent EIS measurements. The EIS measurements were evaluated by the generalized distribution of relaxation times-(gDRT)-analysis.[13,37,47–49]

As a consequence of the charge transfer processes, interfacial resistances, and the electrolyte conductivity an overpotential is induced during plating/stripping experiments.[50] For the SPE20

the overpotential is very low initially (20 mV), but steadily increases asymmetrically to 250 and 450 mV for the different half cycles, respectively. The gDRT analysis shows two main contributions (Figure 5b,c). The ionic conductivity of the bulk electrolyte and the charge transfer resistance across the lithium electrolyte interface can be observed at shorter and longer relaxation times and are denoted as τ_a and τ_b, respectively. With prolonged cycling, the contributing processes for SPE20 (Figure 5b) exhibit slower relaxation times as well as increased polarization (i.e., process resistances) with increasing cycle numbers. Especially the interface resistance contribution (τ_b) increases from 2.8 to 626.9 Ω during plating/stripping for 150 cycles. This indicates that the SPE20 can form intimate contact with the Li-metal anodes, enabling a very efficient charge transfer. However, due to its very soft nature, the deposition and depletion of lithium might occur in an inhomogeneous manner, most likely leading to the formation of mossy or dead lithium agglomerates on the lithium electrode surface, manifesting in increasing overpotentials.

Contrarily, the overpotential for the crosslinked SPE20-SIPN shows a stable overpotential evolution after a short equilibration phase in the first cycles. Throughout the performed cycling experiment up to 150 cycles, the overpotential decreases from 140 to 80 mV. On the other hand, SPE20-SIPN electrolyte exhibits significantly higher initial interfacial resistances of 80 Ω (Figure 5c).
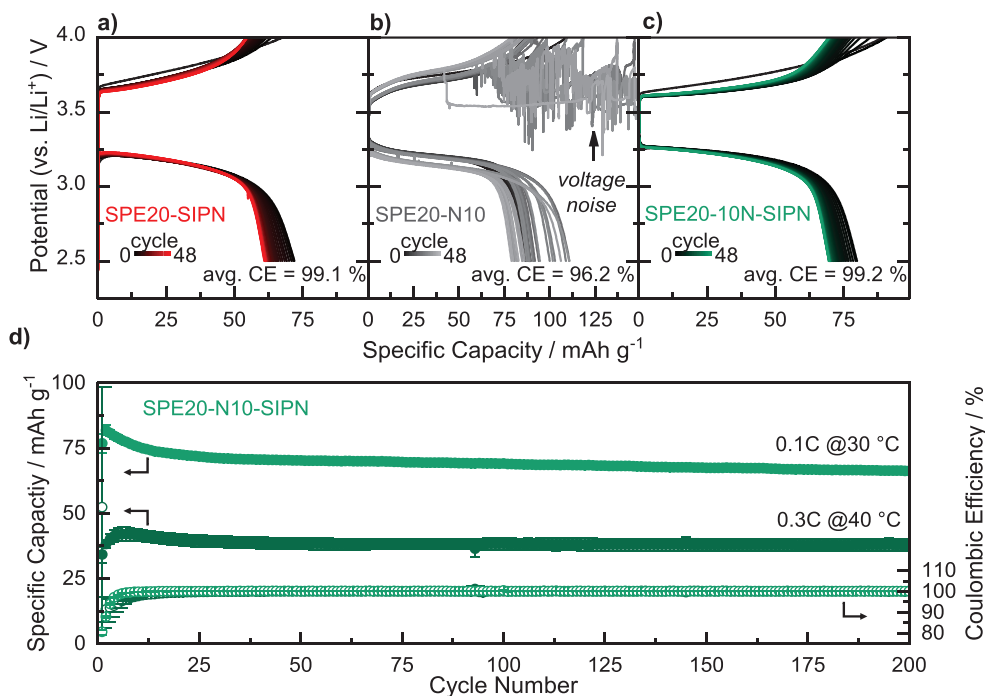
ADVANCED
SCIENCE NEWS

www.advancedsciencenews.com

ADVANCED
ENERGY
MATERIALS

www.advenergymat.de

Figure 6. Battery cycling data in Li|SPE20-SIPN/SPE20-N10/SPE20-N10-SIPN|LFP test cells at a given temperature and C-rate. For all cells, an electrolyte-infiltrated PI7 membrane is used. Data for (red) SPE20-SIPN (SPE20+crosslinking), (gray) SPE20-N10 (SPE20+10 wt.% TiO_2) and (green) SPE20-N10-SIPN (SPE20+10 wt.% TiO_2+crosslinking). Charge and discharge profiles for the three systems, for cycles 0 to 50. Cells were cycled between a) 2.5–4.2 V, b,c) 2.5–4 V. d) Cycling performance (2.5–4.2 V) over 200 charge and discharge cycles of SPE20-N10-SIPN at (green) 0.1C and 30 °C and (dark green) 0.3C and 40 °C. Cycling data in (d) displays an average and corresponding error of three cells.

However, during cycling the interface resistance decreases to 30 Ω, underlining the effective stabilization of the lithium electrolyte interface.

2.5. Battery Application and Cycling Performance

Finally, the cyclability and applicability of the polymer electrolytes were investigated using Li|electrolyte|LFP cells (**Figure 6**). The composition of electrolytes is summarized in Table S5 (Supporting Information). As the electrolyte SPE20 showed significantly increasing charge-transfer resistances in lithium plating and stripping experiments (Figure 5a,b), we did not consider the electrolyte for battery cycling experiments. For the cell fabrication, we have optimized a procedure for low T_g systems using thin polyimide (PI) membrane support.[12,13,51] Thin membranes are of high advantage, as they enable defined and small electrode distances for higher energy densities.[52–54] For this, we soaked a porous polyimide membrane with the electrolyte solution and applied those to the LFP-based cathodes (Figures S13 and S14, Supporting Information). The cell preparation details are given in the Scheme S1 (Supporting Information). A comparative evaluation of the effect of the incorporation of polyimide membrane on the ionic conductivity is provided in Figure S15 (Supporting Information). In samples using PI7 porous membrane, depending on the pressure applied to the coin-cell assembly the thickness can vary between 50 and 120 μm. Therefore, the absolute ionic conductivity values using P17 membrane cannot be obtained in an exact manner as we get it without

the membrane. However, we have measured these conductivities wherever possible and plotted in Figure S15b (Supporting Information).

At first, we investigated the SPE20-SIPN electrolyte at 30 °C and 0.1C (Figure 6a). The cycling performance and electrochemical impedance across different cells are presented in Figure S16 (Supporting Information). It was possible to attain stable charge and discharge profiles for SPE20-SIPN. However, out of four measured cells, two cells showed overcharging or unstable voltage profiles in some of the cycles, where the cut-off potential is not reached but a continuous charging process can be observed (Table S6, Supporting Information). This behavior is also referred to as voltage noise and is ascribed to an unstable lithium-electrolyte interface, resulting in the formation of semi-reversible soft shorts during the charging process.[42] In literature, it was reported that for thin electrolyte layers, such fluctuations can be observed especially for soft electrolytes.[46] However, a variation in electrolyte thickness was not performed in this study.

Another alternative approach to improve the battery cycling characteristics of soft electrolytes is the addition of small amounts of nanoparticles to the electrolyte.[12,48,55,56] Therefore, we wanted to examine if the addition of nanoparticles can improve the crosslinking strategy to avoid the voltage noise phenomena, even in very thin soft electrolytes. This can be easily tested by adding 10 wt.% of TiO_2 to SPE20-SIPN before crosslinking. A comparative evaluation of the effect of the nanoparticle addition and crosslinking on the ionic conductivity is shown in Figure S15 (Supporting Information). The crosslinked nanocomposite electrolyte (SPE20-N10-SIPN) shows extremely

stable battery cycling, where none of the cycles exhibited voltage noise phenomena. An optical image of the cured electrolyte is displayed in Figure S11 (Supporting Information).

For SPE20-N10-SIPN, the discharge capacity stabilized after the first few cycles with average Coulombic efficiencies of 99.1% for the first 50 cycles. The improved efficiency and stable charging and discharging behavior exemplify the significant influence of the network incorporation together with nanoparticle addition and the importance of adequate lithium-electrolyte interface stability. Further, we performed long-term cycling experiments using the SPE20-N10-SIPN electrolyte at different C-rates of 0.1 and 0.3C. Battery cycling at 70 °C (0.1C) exhibits an initial specific capacity of 152.2 ± 3.1 mAh g^{-1} (Figure S17, Supporting Information). Since we aim to develop electrolyte systems working at room temperature, we focused on long-term cycling at reduced temperatures (30 °C and 40 °C). Prior to cycling experiments, no additional pre-cycling was performed. The discharge capacity and Coulombic efficiency for both cycling conditions are depicted in Figure 5d. Both cycling conditions show an equilibration phase of ≈25 cycles after which a stable discharge capacity can be observed. At 0.1C a maximum discharge capacity of 81.8 ± 1.9 mAh g^{-1} was available in the second cycle which decreased to 66.2 ± 1.1 mAh g^{-1} after 200 cycles, representing a capacity retention of 81%. If the equilibration phase (till 25 cycles) is considered as cell conditioning, the capacity retention is above 90%. As expected for increased C-rates accessible discharge capacity was lower at 0.3C and 40 °C. Even though the achieved specific capacity is low, the capacity retention was high in the range of 90%.

On the other hand, a nanocomposite electrolyte without crosslinking (SPE20-N10) showed extreme fluctuations, overcharging, and reduction of the Coulombic efficiency in battery cycling (Figure 6b; Table S6, Supporting Information). These results of battery cycling indicate that a combination of reinforcing strategies is required to enable very thin and soft electrolyte materials. Probably, the strategies adopted such as crosslinking or nanoparticle addition depend on the nature of the electrolyte as well as the electrodes used in the cell setup.

In summary, a combination of crosslinking and addition of nanoparticles enabled stable battery cycling for 200 cycles under different cycling conditions. However, further improvement with regard to increasing the specific capacity at low temperatures and high C-rates is required.

3. Conclusion

We synthesized and studied a SIPN electrolyte system for lithium-metal batteries. The system consists of only ester-based solid polymer electrolytes and crosslinkers. For the SPE we synthesized a low T_g polysiloxane with pendent diester sidechains and used a polyester telechelic for crosslinking. This SPE has a high lithium transfer number in the range of 0.7. The non-crosslinked SPE20 exhibited the highest ionic conductivity of 2.6×10^{-5} S cm^{-1} at 25 °C but showed low mechanical stability and therefore unstable cycling behavior in lithium plating and stripping experiments.

On the other hand, the crosslinked electrolyte system (SPE20-SIPN) maintains the high ionic conductivity while also having significantly improved mechanical properties. The semi-interpenetrating network structure (PM(BMA)S-SIPN) showed a predominantly elastic behavior ($G' > G''$) and induced significantly improved mechanical stability (from 2 Pa to 4250 Pa) compared to the non-crosslinked blend, demonstrating the effect of the network-establishment. Consequently, stable lithium electrolyte interfaces, low charge transfer resistances, and stable overpotentials could be achieved in lithium plating and stripping experiments. As a result of this, SPE20-SIPN is suitable for battery cycling in combination with lithium-metal anodes and LFP-base composite cathodes. For its application at room temperature addition of nanoparticles enabled long-term stable cycling with high Coulombic efficiency. Lithium plating and stripping clearly shows the influence and advantage of the crosslinking strategy leading to SIPN electrolytes. The increasing overpotential in SPE20 could be stabilized in SPE20-SIPN. Similarly, in battery cycling the advantage of SIPN is obvious. For example, in SPE20-N10 (reinforcing with nanoparticles, but without any crosslinking) no stable cycling could be observed. On the other hand, when the SIPN strategy is used for SPE20-SIPN and SPE20-N10-SIPN the overcharging issues could be prevented clearly demonstrating the importance of SIPN also for battery cycling even in the presence of PI7 membrane. Thus, a combination of low T_g electrolyte, crosslinking, and nanoparticle addition strategy (SPE20-N10-SIPN) offers benefits for low-temperature battery applications, especially in thin all solid state batteries.

4. Experimental Section

Electrolyte Formulation: The polysiloxane-based electrolytes (SPEXX, XX = LiTFSI wt%) were prepared by combining the PM(BMA)S polymer and LiTFSI in acetonitrile at different weight proportions (10–50 wt.% LiTFSI). The solution was allowed to stir overnight. Afterward, the solvent is removed under reduced pressure at 80 °C overnight. The SPE-SIPN was prepared by dissolving PM(BMA)S, PCLDA, LiTFSI, and AIBN in acetonitrile. The solution was stirred overnight. Drying was conducted only at RT over two days in high vacuum. Dried electrolytes were used for IC, LSV, LPS, LTN experiments. For SPE20-N10 (SPE20+10 wt.% TiO$_2$ nanoparticles) and SPE20-N10-SIPN (SPE20-SIPN+10 wt.% TiO$_2$ nanoparticles) the nanoparticles are dispersed in acetonitrile using a ultrasonication for 30 minutes. Afterward, the remaining constituents are added and processed under the same conditions. Electrolytes used in battery cells (Li|electrolyte|cathode) are not dried but used as solution during cell preparation. The exact composition of the electrolytes is given in Tables S1 and S5 (Supporting Information).

Annealing and Crosslinking: For test cells (IC, LSV, LPS, LTN) dried electrolytes are used during cell preparation. After sealing the cells inside an Ar-filled glovebox the cells are transferred to an oven at 100 °C overnight for annealing. For all cells using SPE20-SIPN or SPNE20-N10-SIPN the annealing step at 100 °C leads to the in-situ formation of the crosslinked system inside the cell. For all battery (Li-SPE-cathode) cells, cathode-supported electrolytes are employed (see chapter 4.4). Crosslinking is also achieved during the drying/curing step at 100 °C overnight under high vacuum. Indeed, AIBN can be applied at more moderate conditions compared to 100 °C. Additionally, as the cathode-supported electrolyte is dried and crosslinked in the same step under high vacuum, the study wants to ensure quantitative removal of the solvent from the electrolyte to obtain a dry solid polymer electrolyte. Therefore, a temperature of 100 °C was used. The experimental procedure for crosslinking during rheology measurements is explained in the supporting information.

Cathode Formulation: The cathodes were prepared by dispersing the cathode constituents in a combination of acetonitrile and N-methyl pyrrolidone (1:2 vol). 2.1 mL of solvent mixture was used per 1 g of active

**ADVANCED
SCIENCE NEWS**

www.advancedsciencenews.com

**ADVANCED
ENERGY
MATERIALS**

www.advenergymat.de

material. The cathode composition was active material: carbonaceous additives (super P carbon and graphitic carbon): PVDF binder: SPE20 electrolyte = 70:10:15:5. The cathode mixture is homogenized by ball milling for 1.5 h (9 cycles of 10 min milling and 10 min resting phase). The cathode slurry was coated onto carbon-coated aluminum current collectors by doctor blade technique with a gap height of 380 μm. The cathode laminates were left to passively dry overnight. Afterward, the cathodes were transferred to a vacuum oven for further drying at 80 °C under high vacuum overnight. The cathode laminate is densified at 60 °C by applying stepwise increasing pressure of 1, 2, 3, and 4 tons for 2 minutes at each pressure. The cathodes were punched into discs with a diameter of 14 mm (area 1.54 cm^2). The active material mass loading was ≈3.2 mg cm^{-2} (0.54 mAh cm^{-2}).

Cell Fabrication: All electrochemical measurements were conducted using CR2032-type coin cells. For the determination of the ionic conductivity (IC), stainless steel (StSt) blocking electrodes were used (StSt|electrolyte|StSt). For linear sweep voltammetry (LSV) measurements StSt working electrode (WE) and lithium as reference and counter electrode (RE and CE) was used (StSt|electrolyte|Li). The lithium transference number (LTN) determination and lithium plating and stripping (LPS) was conducted using symmetrical lithium cells (Li|electrolyte|Li). For IC, LSV, LTN, and LSV measurements a Kapton spacer (thickness 130 μm, diameter 16 mm) with a hole of defined diameter (4 mm) was used. Kapton spacers are used to establish defined and controlled cell geometries (thickness and area) and to avoid uncontrolled pressing during cell preparation using soft electrolytes. Of course, it may not be necessary if sufficient thickness and mechanical integrity is guaranteed for the soft electrolyte. But highly reproducible results were obtained using such gaskets and it saved novel materials by limiting the area and thickness in a controlled manner. The cavity is filled with electrolyte during coin cell assembly. For battery test cells consisting of lithium metal and the prepared cathodes (Li|electrolyte|LFP) a track-etched polyimide separator (porosity 28%) with a thickness of 7 μm (PI7) was used. The separator was preheated and a thin coating of an electrolyte solution was applied. After two minutes the semi-coated separator was placed on a cathode disc with the electrolyte coating facing the electrode. Subsequently, the uncoated separator was also coated with the electrolyte solution. The assembly of the cathode and electrolyte-infiltrated separator was dried at 100 °C under high vacuum and then transferred to a glovebox. There lithium-metal anodes (diameter 14 mm) are applied.

Electrochemical Measurements: Electrochemical impedance spectroscopy (EIS) was conducted in a frequency range of 3 MHz – 0.1 Hz with a sinusoidal excitation potential of 20 mV. A climate chamber was used for temperature-dependent EIS measurements. IC cells were annealed at 70 °C for 12 h. Afterward, the individual measurements were taken at 60, 80, 70, 60, 50, 40, 30, and 25 °C after an equilibration period of 1.5 h for each temperature step. All other electrochemical test cells were annealed at the temperature of the subsequent measurement: LTN, LSV, LPS, GO at 70 °C for 12 h at OCV; battery cycling at 30 °C or 40 °C for 5 hours at OCV. Linear sweep voltammetry was conducted between 0 and 6 V at a scan rate of 0.1 mV s^{-1}. Lithium transference number determinations were performed following the Bruce and Vincent method consisting of an initial EIS measurement, a chronoamperometric polarization (potential 10 mV, duration 3 h), and a second EIS measurement immediately after the polarization interval. Lithium plating and stripping (LPS) experiments were performed using a current density of 0.1 mA cm^{-2} with a half-cycle duration of 1 h. Every 5 full cycles the LPS was stopped to perform an EIS measurement. Before galvanostatic overcharging, three battery cycles at 0.1 C (2.6–4.0 V) were performed. Afterward, the cell is charged without a cut-off at 0.1 C. Further battery cycling was conducted between 2.5 and 4.2 V using different C-rates and temperatures (0.1C at 30 °C, 0.3C at 40 °C).

Supporting Information

Supporting Information is available from the Wiley Online Library or from the author.

Conflict of Interest

The authors declare no conflict of interest.

Author Contributions

J.P. conceptualized the idea for the study; wrote the original draft; performed synthesis; designed the methodology; performed investigation; and visualized the idea for the study. M.D. performed the synthesis; designed the methodology; and performed the investigation. M.T. performed the funding acquisition, project administration, and supervision; and wrote, reviewed, and edited the manuscript. The manuscript was written through the contributions of all authors. All authors have given approval to the final version of the manuscript.

Data Availability Statement

The data that support the findings of this study are available from the corresponding author upon reasonable request.

[1] W. Xu, J. Wang, F. Ding, X. Chen, E. Nasybulin, Y. Zhang, J.-G. Zhang, *Energy Environ. Sci.* **2014**, *7*, 513.

[2] G. Bieker, M. Winter, P. Bieker, *Phys. Chem. Chem. Phys.* **2015**, *17*, 8670.

[3] K. J. Harry, K. Higa, V. Srinivasan, N. P. Balsara, *J. Electrochem. Soc.* **2016**, *163*, A2216.

[4] P. Barai, K. Higa, V. Srinivasan, *Phys. Chem. Chem. Phys.* **2017**, *19*, 20493.

[5] L. Stolz, M. Winter, J. Kasnatscheew, *J. Electrochem. Sci. Eng.* **2023**, *13*, 715.

[6] D. Zhang, L. Li, X. Wu, J. Wang, Q. Li, K. Pan, J. He, *Front. Energy Res.* **2021**, *9*, 726738.

[7] H. Wang, L. Sheng, G. Yasin, L. Wang, H. Xu, X. He, *Energy Storage Mater.* **2020**, *33*, 188.

[8] X. Yu, Z. J. Hoffman, J. Lee, C. Fang, L. A. Gido, V. Patel, H. B. Eitouni, R. Wang, N. P. Balsara, *ACS Energy Lett.* **2022**, *7*, 3791.

[9] M. P. Rosenwinkel, R. Andersson, J. Mindemark, M. Schönhoff, *J. Phys. Chem. C* **2020**, *124*, 23588.

[10] K. M. Diederichsen, E. J. McShane, B. D. McCloskey, *ACS Energy Lett.* **2017**, *2*, 2563.

[11] L. Stolz, G. Homann, M. Winter, J. Kasnatscheew, *Mater. Today* **2021**, *44*, 9.

[12] D. Rosenbach, A. Krimalowski, H. Erabhoina, M. Thelakkat, *J. Mater. Chem. A* **2022**, *10*, 8932.

[13] A. Krimalowski, D. Rosenbach, H. Erabhoina, M. Thelakkat, *J. Energy Storage* **2023**, *65*, 107348.

[14] T. Eriksson, A. Mace, J. Mindemark, D. Brandell, *Phys. Chem. Chem. Phys.* **2021**, *23*, 25550.

[15] R. Andersson, G. Hernández, J. Mindemark, *Phys. Chem. Chem. Phys.* **2022**, *24*, 16343.

[16] L. Imholt, T. S. Dörr, P. Zhang, L. Ibing, I. Cekic-Laskovic, M. Winter, G. Brunklaus, *J. Power Sources* **2019**, *409*, 148.

[17] Y.-H. Chen, Y.-C. Hsieh, K. L. Liu, L. Wichmann, J. H. Thienenkamp, A. Choudhary, D. Bedrov, M. Winter, G. Brunklaus, *Macromol. Rapid Commun.* **2022**, *43*, 2200335.

[18] T. Eriksson, J. Mindemark, M. Yue, D. Brandell, *Electrochim. Acta* **2019**, *300*, 489.

[19] D. Pei, Y. Li, S. Huang, M. Liu, J. Hong, S. Hou, H. Jin, G. Cao, *Chem. Eng. J.* **2023**, *461*, 141899.

[20] Y.-H. Chen, P. Lennartz, K. L. Liu, Y.-C. Hsieh, F. Scharf, R. Guerdelli, A. Buchheit, M. Grünebaum, F. Kempe, M. Winter, G. Brunklaus, *Adv. Funct. Mater.* **2023**, *33*, 2300501.

[21] A. J. Butzelaar, K. L. Liu, P. Röring, G. Brunklaus, M. Winter, P. Theato, *ACS Appl. Polym. Mater.* **2021**, *3*, 1573.

[22] O. Mukbaniani, G. Titvinidze, A. Dundua, M. Doroshenko, T. Tatrishvili, *J. Appl. Polym. Sci.* **2008**, *107*, 2567.

[23] M. Suguro, A. Mori, S. Iwasa, K. Nakahara, K. Nakano, *Macromol. Chem. Phys.* **2009**, *210*, 1402.

[24] D. He, X. Gui, S. Dong, Y. Lin, Y. Tu, J. Hu, S. Li, J. Zhao, *Polym. Adv. Technol.* **2023**, *34*, 1979.

[25] M. S. Grewal, M. Tanaka, H. Kawakami, *Electrochim. Acta* **2019**, *307*, 148.

[26] Z. C. Zhang, J. J. Jin, F. Bautista, L. J. Lyons, N. Shariatzadeh, D. Sherlock, K. Amine, R. West, *Solid State Ionics* **2004**, *170*, 233.

[27] C. Fu, M. Iacob, Y. Sheima, C. Battaglia, L. Duchêne, L. Seidl, D. M. Opris, A. Remhof, *J. Mater. Chem. A* **2021**, *9*, 11794.

[28] D. Fish, I. M. Khan, E. Wu, J. Smid, *Br. Polym. J.* **1988**, *20*, 281.

[29] B. Oh, D. Vissers, Z. Zhang, R. West, H. Tsukamoto, K. Amine, *J. Power Sources* **2003**, *119–121*, 442.

[30] K. H. Min, D. B. Kim, Y. K. Kang, D. H. Suh, *J. Appl. Polym. Sci.* **2008**, *107*, 1609.

[31] X.-X. Zeng, Y.-X. Yin, N.-W. Li, W.-C. Du, Y.-G. Guo, L.-J. Wan, *J. Am. Chem. Soc.* **2016**, *138*, 15825.

[32] P. Chen, X. Liu, S. Wang, Q. Zeng, Z. Wang, Z. Li, L. Zhang, *ACS Appl. Mater. Interfaces* **2019**, *11*, 43146.

[33] R. Khurana, J. L. Schaefer, L. A. Archer, G. W. Coates, *J. Am. Chem. Soc.* **2014**, *136*, 7395.

[34] C. P. Fonseca, D. S. Rosa, F. Gaboardi, S. Neves, *J. Power Sources* **2006**, *155*, 381.

[35] J. Mindemark, B. Sun, E. Törmä, D. Brandell, *J. Power Sources* **2015**, *298*, 166.

[36] K. Zalewski, Z. Chyłek, W. A. Trzciński, *Polymers* **2021**, *13*, 1080.

[37] M. Hahn, D. Rosenbach, A. Krimalowski, T. Nazarenus, R. Moos, M. Thelakkat, M. A. Danzer, *Electrochim. Acta* **2020**, *344*, 136060.

[38] K. M. Diederichsen, H. G. Buss, B. D. McCloskey, *Macromolecules* **2017**, *50*, 3831.

[39] J. Evans, C. A. Vincent, P. G. Bruce, *Polymer* **1987**, *28*, 2324.

[40] T. Eriksson, H. Gudla, Y. Manabe, T. Yoneda, C. Friesen, C. Zhang, Y. Inokuma, D. Brandell, J. Mindemark, *Macromolecules* **2022**, *55*, 10940.

[41] S. A. Krachkovskiy, J. D. Bazak, P. Werhun, B. J. Balcom, I. C. Halalay, G. R. Goward, *J. Am. Chem. Soc.* **2016**, *138*, 7992.

[42] G. Homann, L. Stolz, M. Winter, J. Kasnatscheew, *iScience* **2020**, *23*, 101225.

[43] P.-M. Jalbert, B. Commarieu, J.-C. Daigle, J. P. Claverie, K. Zaghib, *J. Electrochem. Soc.* **2020**, *167*, 080527.

[44] I. Aldalur, M. Martinez–Ibañez, M. Piszcz, H. Zhang, M. Armand, *Batteries Supercaps* **2018**, *1*, 149.

[45] G. Hernández, I. L. Johansson, A. Mathew, C. Sångeland, D. Brandell, J. Mindemark, *J. Electrochem. Soc.* **2021**, *168*, 100523.

[46] G. Homann, L. Stolz, J. Nair, I. C. Laskovic, M. Winter, J. Kasnatscheew, *Sci. Rep.* **2020**, *10*, 4390.

[47] M. Hahn, S. Schindler, L.-C. Triebs, M. A. Danzer, *Batteries* **2019**, *5*, 43.

[48] H. Erabhoina, D. Rosenbach, J. Mohanraj, M. Thelakkat, *Electrochim. Acta* **2021**, *387*, 138455.

[49] C. Plank, T. Rüther, L. Jahn, M. Schamel, J. P. Schmidt, F. Ciucci, M. A. Danzer, *J. Power Sources* **2023**, *594*, 233845.

[50] K.-H. Chen, K. N. Wood, E. Kazyak, W. S. LePage, A. L. Davis, A. J. Sanchez, N. P. Dasgupta, *J. Mater. Chem. A* **2017**, *5*, 11671.

[51] J. Petry, H. Erabhoina, M. Dietel, M. Thelakkat, *ACS Appl. Polym. Mater.* **2024**, *6*, 5109.

[52] S. Zhong, B. Yuan, Z. Guang, D. Chen, Q. Li, L. Dong, Y. Ji, Y. Dong, J. Han, W. He, *Energy Storage Mater.* **2021**, *41*, 805.

[53] Z. Wang, L. Shen, S. Deng, P. Cui, X. Yao, *Adv. Mater.* **2021**, *33*, 2100353.

[54] J. Wu, L. Yuan, W. Zhang, Z. Li, X. Xie, Y. Huang, *Energy Environ. Sci.* **2021**, *14*, 12.

[55] X. Judez, M. Piszcz, E. Coya, C. Li, I. Aldalur, U. Oteo, Y. Zhang, W. Zhang, L. M. Rodriguez-Martinez, H. Zhang, M. Armand, *Solid State Ionics* **2018**, *318*, 95.

[56] C. Fu, V. Venturi, J. Kim, Z. Ahmad, A. W. Ells, V. Viswanathan, B. A. Helms, *Nat. Mater.* **2020**, *19*, 758.